



# Six-Pulse RIDME Sequence to Avoid Background Artifacts

Dinar Abdullin<sup>1</sup> · Miriam Suchatzki<sup>1</sup> · Olav Schiemann<sup>1</sup> 

Received: 13 November 2020 / Revised: 12 March 2021 / Accepted: 21 March 2021 /  
Published online: 9 April 2021  
© The Author(s) 2021

## Abstract

Relaxation induced dipolar modulation enhancement (RIDME) is a valuable method for measuring nanometer-scale distances between electron spin centers. Such distances are widely used in structural biology to study biomolecular structures and track their conformational changes. Despite significant improvements of RIDME in recent years, the background analysis of primary RIDME signals remains to be challenging. In particular, it was recently shown that the five-pulse RIDME signals contain an artifact which can hinder the accurate extraction of distance distributions from RIDME time traces [as reported by Ritsch et al. (Phys Chem Chem Phys 21: 9810, 2019)]. Here, this artifact, as well as one additionally identified artifact, are systematically studied on several model compounds and the possible origins of both artifacts are discussed. In addition, a new six-pulse RIDME sequence is proposed that eliminates the artifact with the biggest impact on the extracted distance distributions. The efficiency of this pulse sequence is confirmed on several examples.

## 1 Introduction

Nanometer-scale distance measurements using electron paramagnetic resonance (EPR) spectroscopy provide important information for studying the structure and conformational states of biomacromolecules, such as proteins, nucleic acids, and their complexes [1]. In particular, several pulsed EPR techniques, such as pulsed electron–electron double resonance (PELDOR or DEER) [2, 3], double quantum coherence EPR (DQC) [4], single-frequency technique for refocusing dipolar couplings (SIFTER) [5], and relaxation induced dipolar modulation enhancement (RIDME) [6, 7], are widely used to measure distances in the range of 1.5–16 nm. These techniques have no limitation on the size of a biomolecule and are applicable to biomolecules in solution [8], within membranes [9] or whole cells [10–12]. Among the techniques mentioned, PELDOR is probably the most widely used. This stems from the fact that it is well suited for distance measurements between

---

✉ Olav Schiemann  
schiemann@pc.uni-bonn.de

<sup>1</sup> University of Bonn, Institute of Physical and Theoretical Chemistry, Bonn, Germany

nitroxide spin labels, which can be bound to the surface of a biomolecule in a site-specific manner [13]. When applied to other types of spin centers, PELDOR can become more difficult and less efficient than other EPR techniques. For example, DQC and SIFTER outperform PELDOR in terms of modulation depth and sensitivity for spin labels with spectral widths comparable to microwave pulse bandwidths [14], such as trityl-based spin labels [11, 15–17]. These advantages make it possible to perform DQC measurements on trityl-labeled proteins at concentrations as low as 90 nM [11]. In addition, the five-pulse RIDME (5p-RIDME, Fig. 1a) sequence has been shown to have advantages over PELDOR when applied to spin centers with spectral widths that significantly exceed the bandwidths of microwave pulses, such as  $\text{Cu}^{2+}$  [18–24],  $\text{Gd}^{3+}$  [24–28],  $\text{Mn}^{2+}$  [24, 29, 30],  $\text{Co}^{2+}$  [31], low-spin, and high-spin  $\text{Fe}^{3+}$  [32–35]. For all these metal ions, RIDME provides significantly larger modulation depth and thus better sensitivity compared to PELDOR [36, 37]. For example, Q-band RIDME experiments on the spin pair  $\text{Cu}^{2+}$ -nitroxide yielded about 100 times higher sensitivity than the corresponding PELDOR experiment with rectangular pulses, allowing RIDME measurements at submicromolar concentrations

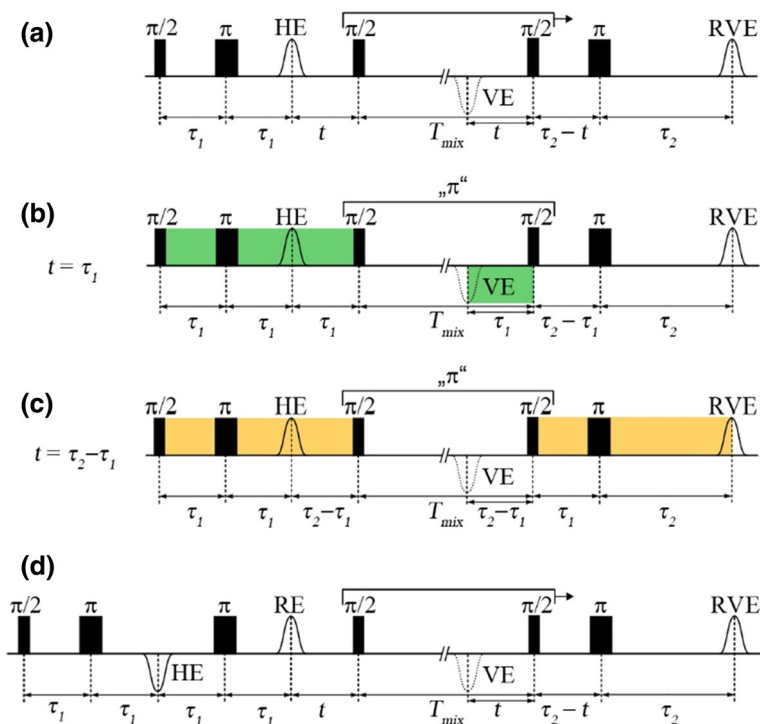


**Fig. 1** RIDME pulse sequences. **a** The 5p-RIDME sequence. The primary Hahn echo is denoted HE, the virtual echo VE, and the refocused virtual echo RVE. **b** The 5p-RIDME sequence for the case of  $t = \tau_1$ . The inter-pulse time intervals of the Carr–Purcell subsequence are shown in green. **c** The 5p-RIDME sequence for the case of  $t = \tau_2 - \tau_1$ . The inter-pulse intervals before and after the mixing block are also shown in orange. **d** The 6p-RIDME sequence with refocused Hahn echo denoted as RE, and the other echoes being identical to those of the five-pulse sequence (color figure online)

[21]. Moreover, RIDME also allows to avoid orientation selectivity [38], for at least one of the dipolar coupled spins, which simplifies the conversion of a primary RIDME signal, called a RIDME time trace, into a distance distribution. RIDME is particularly well suited for spin pairs consisting of a metal center and a nitroxide or trityl spin label. For such spin pairs, the RIDME time trace is acquired on a slowly relaxing organic radical, while a rapidly relaxing metal center is flipped by spontaneous relaxation [18, 20, 29, 33–35]. Acquiring the time trace on the slow-relaxing organic radical results in a good signal-to-noise ratio (SNR), and the nonselective inversion of the metal center by spontaneous relaxation maximizes the modulation depth and avoids orientation selectivity for the metal centers. Thus, RIDME enables effective distance measurements between several, spectroscopically different spin centers [18, 39, 40]. Moreover, RIDME measurements between metal ions and organic spin labels are relevant for the localization of metal cofactors in biomolecules [41, 42].

Despite numerous advantages, some aspects of RIDME-based distance measurements require further consideration. One of these is the background analysis. The goal of the background analysis is to remove an unmodulated decay from a primary RIDME time trace. The main contribution to this decay comes from spin diffusion [36]. Unlike the PELDOR background, the RIDME background cannot be described by a monoexponential decay. Keller et al. derived a theoretical expression for the 5p-RIDME background that contains the product of monoexponential and Gaussian decays [24]. However, experimental studies emphasized that the background decay is better described by one or two stretched exponential decays [24]. In addition to the stretched exponential function, polynomial functions have been shown to provide adequate fits to RIDME backgrounds [33–35]. The difference between the theory and the experiments is likely due to the simplifications used to derive the theoretical expression. In addition to the complicated shape of the 5p-RIDME background, Ritsch et al. reported an artifact that occurred repeatedly in 5p-RIDME backgrounds measured on a nitroxide monoradical and a nitroxide-Cu<sup>2+</sup> compound [20]. This artifact was shown to have an effect on the shape of the 5p-RIDME time traces and introduce errors into the distance distributions. Although an accurate description of the artifact is required, the nature of this artifact still remains unclear. So far, it has been shown that it is not an echo-crossing artifact and that it disappears for a sufficiently long inter-pulse time interval  $\tau_1$  ( $\tau_1 = 3.5 \mu\text{s}$ ) [20]. However, since the amplitude of the 5p-RIDME signal decreases in the time interval  $2\tau_1$  with the transversal relaxation time, the proposed method for removing the background artifact results in significant losses in SNR and reduces the maximal accessible distance.

In the work presented here, the origin of the background artifact is identified and a new six-pulse RIDME sequence (6p-RIDME, Fig. 1d) is proposed for suppressing it. The performance of this sequence is tested on a nitroxide monoradical **1**, a nitroxide biradical **2**, and two low-spin Fe<sup>3+</sup>-nitroxide model compounds, **3** and **4** (Fig. 2).

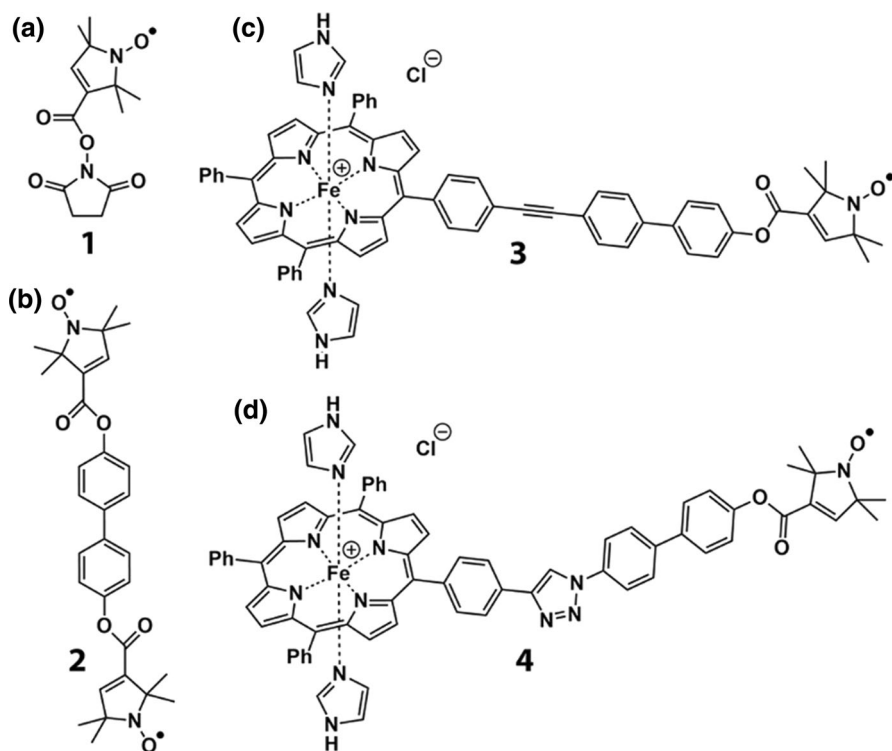


**Fig. 2** Chemical structures of compounds used for RIDME experiments. **a** Nitroxide monoradical **1**. **b** Nitroxide biradical **2**. **c, d** Low-spin  $\text{Fe}^{3+}$ -nitroxide model compounds **3** and **4**

## 2 Experimental

### 2.1 Test Systems

Nitroxide monoradical **1** (Fig. 2a) was purchased from Cayman Chemicals. For the RIDME measurements, 50 or 200  $\mu\text{M}$  of **1** were dissolved in three different solvents: 1) deuterated TES buffer (0.1 M TES pH 7.5, 100 mM NaCl in  $\text{D}_2\text{O}$ ) containing 20 v/v% glycerol- $\text{d}_8$ , 2) toluene- $\text{d}_8$  (Deutero), and 3) THF- $\text{d}_8$  (Deutero).

The synthesis of nitroxide biradical **2** (Fig. 2b) has been reported previously [43]. RIDME measurements were performed on 200  $\mu\text{M}$  of **2** dissolved in deuterated toluene.

The synthesis of low-spin  $\text{Fe}^{3+}$ -nitroxide model compounds **3** (Fig. 2c) and **4** (Fig. 2d) has also been reported previously [34, 44]. Both compounds were dissolved in deuterated THF and had a concentration of 200  $\mu\text{M}$ .

## 2.2 RIDME Experiments

Relaxation induced dipolar modulation enhancement measurements were performed on a Bruker ELEXSYS E580 spectrometer using a Flexline probe head with a Q-band resonator ER5106QT-2 (Bruker). Microwave pulses were amplified using a 150 W TWT amplifier (Applied Systems Engineering, model 187Ka). To obtain temperatures of 12–50 K, the resonator was mounted into a continuous flow helium cryostat CF935 (Oxford Instruments), and the temperature inside the cryostat was adjusted by a temperature control system ITC 503 (Oxford Instruments).

Relaxation induced dipolar modulation enhancement experiments were performed using an established five-pulse sequence  $\pi/2-\tau_1-\pi-(\tau_1+t)-\pi/2-T_{mix}-\pi/2-(\tau_2-t)-\pi-\tau_2$ -echo [7], as well as a new six-pulse sequence  $\pi/2-\tau_1-\pi-2\tau_1-\pi-(\tau_1+t)-\pi/2-T_{mix}-\pi/2-(\tau_2-t)-\pi-\tau_2$ -echo (see SE, Chapter 1 for the PulseSPeL program). The frequency of the microwave pulses was set in resonance with the maximum of the nitroxide spectrum. The lengths of the  $\pi/2$  and  $\pi$  pulses were 12 and 24 ns, respectively. The initial value of  $\tau_1$  was set to various values, ranging from 100 ns to 4  $\mu$ s, while the initial value of  $\tau_2$  was kept constant at 3.5  $\mu$ s. To suppress deuterium electron spin echo envelop modulation ( $^2\text{H}$  ESEEM), the initial values of  $\tau_1$  and  $\tau_2$  were increased simultaneously and stepwise with an increment  $\Delta\tau=8$  ns and a number of steps  $m=16$ , resulting in a total of 16 averaging cycles [26].  $T_{mix}$  was set to 100  $\mu$ s, which has been shown to be the optimal mixing time at 12 K in the earlier RIDME studies on **3** and **4** [34]. For consistency, the same  $T_{mix}$  value and the same temperature were used for the RIDME measurements on **1**. For **2**,  $T_{mix}$  was set to 200  $\mu$ s and the measurements were performed at 50 K instead of 12 K (see SI, Chapter 5). During the RIDME experiments,  $t$  was linearly incremented from -40 ns to 3400 ns with a step of 8 ns, yielding 430 data points in total. The shot repetition time was set to 10 ms. To avoid overlap of unwanted echoes with the detected refocused virtual echo, 8-step [7] and 32-step (see SI, Chapter 2) phase cycling schemes were used for the 5p- and 6p-RIDME sequences, respectively. As a result, the duration of each five- and six-pulse RIDME experiments was approximately 10 and 40 min, respectively. All 5p- and 6p-RIDME time traces were averaged over 8 and 2 scans, respectively.

## 2.3 RIDME Data Analysis

Background correction of all experimental RIDME time traces was performed using the program *DeerAnalysis2019* [45]. The background was fitted using a fourth-order polynomial function (see explanation below). The Fourier transform of the background-corrected RIDME time traces was done using the home-written Python script *fft.py* ([www.github.com/dinarabdullin/Python-scripts-for-EPR/](http://www.github.com/dinarabdullin/Python-scripts-for-EPR/)).

Distance distributions were extracted from the RIDME time traces of **2** using the Tikhonov regularization implemented in *DeerAnalysis2019*. The regularization parameter  $\alpha$  was determined based on the L-curve criterion and fell within the range of 2–5. The error of the *DeerAnalysis*-based distance distributions was estimated using the validation tool. In each validation run, the noise level and the starting

position for the background correction were varied in the range [1.0, 1.5] of the original noise level (10 trials) and [50 ns, 500 ns] (50 trials), respectively.

For **3** and **4**, the program *AnisoDipFit* [46] was used to extract distance and angle distributions from RIDME time traces.

### 3 Results and Discussion

#### 3.1 RIDME Background Measurements on the Nitroxide Monoradical

According to the report by Ritsch et al. [20], when the 5p-RIDME signal is acquired on nitroxide spin centers, the corresponding time trace contains a background artifact whose position depends on the inter-pulse interval  $\tau_1$ . Here, this artifact was investigated for nitroxide monoradical **1**. First, the RIDME time traces were recorded on 200  $\mu\text{M}$  of **1** in deuterated TES buffer using different values of  $\tau_1$  (Fig. 3). Interestingly, the time traces that were measured with  $\tau_1 < \tau_2$  have a non-monotonic decay with prominent peaks at one or two time points (green and red

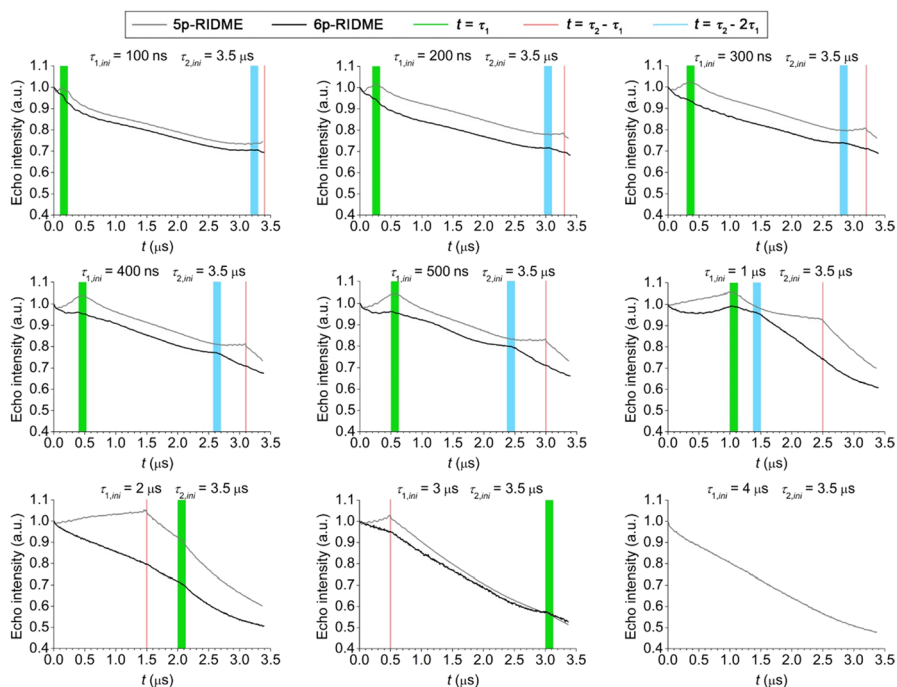


**Fig. 3** Q-band 5p-RIDME (gray lines) and 6p-RIDME (black lines) time traces of **1** as a function of time interval  $\tau_1$ . The corresponding initial values of  $\tau_1$  and  $\tau_2$ , denoted as  $\tau_{1,ini}$  and  $\tau_{2,ini}$ , are given above each time trace. The time points corresponding to  $t = \tau_1$ ,  $t = \tau_2 - \tau_1$ , and  $t = \tau_2 - 2\tau_1$  are shown as green, red, and blue regions, respectively. Since each RIDME time trace was averaged over several different values of  $\tau_1$  and  $\tau_2$  for the  $^2\text{H}$ -ESEEM suppression, the time points  $t = \tau_1$  are shown as bars having a width of the ESEEM averaging interval (color figure online)

bars in Fig. 3). These peaks are surprising because in the absence of intra-molecular dipole–dipole coupling, the 5p-RIDME signal is expected to decay monotonically due to spin diffusion of the detected spins. Therefore, the obtained peaks are referred as “artifacts”. The analysis of the artifact positions for different  $\tau_1$  values shows that all artifacts occur at two defined values of  $t$ , namely  $t = \tau_1$  and  $t = \tau_2 - \tau_1$  (green and red bars in Fig. 3). Since the values of  $\tau_1$  and  $\tau_2$  were simultaneously incremented in each single RIDME experiment for the  $^2\text{H}$ -ESEEM averaging, the artifact at  $t = \tau_1$  is distributed over the interval  $t = (\tau_{1,ini} + m \cdot \Delta\tau)$ , where  $\tau_{1,ini}$  is the initial value of  $\tau_1$ , and  $\Delta\tau$  and  $m$  are the magnitude and the number of  $\tau_1$  increments, respectively. As the same increment  $\Delta\tau$  was used for  $\tau_1$  and  $\tau_2$ , the artifact at  $t = \tau_2 - \tau_1$  has the same position for all  $\tau_1$  and  $\tau_2$  values. Note that the obtained dependence of the artifact positions on  $\tau_1$  and  $\tau_2$  explains why no artifacts were observed for the case  $\tau_1 > \tau_2$  (Fig. 3). Further 5p-RIDME experiments on **1** showed that both artifacts prevail if 1) the temperature of the RIDME experiment is increased from 12 to 50 K (Figure S3), 2) different  $T_{mix}$  values are used (Figure S4), 3) different repetition rates are used, including those that are significantly longer than the spin–lattice relaxation rate of **1** (Figure S5), 4) different integration window widths are used for measuring the RIDME echo intensity (Figure S6), 5) the concentration of **1** is reduced from 200 to 50  $\mu\text{M}$  (Figure S7), and 6) other solvents, such as deuterated THF or toluene, are used (Figure S8). The experiments with different solvents revealed that the intensity of both background artifacts depends on the type of solvent. The highest intensity of the artifacts is obtained in TES buffer, and the lowest intensity in THF. The most likely reason for this difference is the different degree of nuclear spin diffusion in these solvents (Figure S9). The artifact at  $t = \tau_1$ , but not the artifact at  $t = \tau_2 - \tau_1$ , was also obtained in the 5p-RIDME time traces recorded on the refocused stimulated echo (RSE) instead of the refocused virtual echo (RVE) (Figure S10). The absence of the second artifact in the RSE-detected RIDME time traces is discussed below.

To develop methods to eliminate both artifacts in the RIDME background, the origin of the artifacts has to be determined. One of the most common reasons for artifacts in pulsed EPR data is echo crossing. However, echo crossing was excluded earlier by the detailed analysis of all coherence paths in the RIDME experiment [20]. Here, the previous result could be confirmed theoretically and experimentally (see SI, Chapter 2). Most likely, effects such as spin diffusion and ESEEM are also not the cause of the artifacts. Alternatively, the artifacts could be related to the refocusing of hyperfine interactions in the 5p-RIDME experiment. It is known that this process can be influenced by dynamical decoupling. Dynamical decoupling is obtained, for example, in the Carr–Purcell sequences [47, 48], which use repeated refocusing to suppress spin coherence decay caused by nuclear spin diffusion. The simplest Carr–Purcell sequence is  $\pi/2-\tau-\pi-2\tau-\pi-\tau$ -echo, where the spacing between the two refocusing  $\pi$ -pulses is twice the spacing between the first  $\pi/2$ - and  $\pi$ -pulses. When  $t = \tau_1$  in the 5p-RIDME sequence and one considers the mixing block  $\pi/2-T_{mix}-\pi/2$  as an effective  $\pi$ -pulse, one can recognize that the first four pulses of the 5p-RIDME sequence form the Carr–Purcell sequence discussed above (green bars in Fig. 1b). Note that the spacing between the pulses required to obtain the Carr–Purcell sequence is achieved only at  $t = \tau_1$ . This explains why the amplitude of the RIDME background increases at  $t = \tau_1$ , giving rise to one of the artifacts. In

addition, dynamical decoupling can be expected to influence the amplitude of the detected echo even for  $t$  values that only approach the condition  $t = \tau_1$ . This is in a good agreement with the fact that the artifact at  $t = \tau_1$  has a quite significant width of 500–800 ns.

The origin of the second artifact at  $t = \tau_2 - \tau_1$  is less clear. The key to explain this artifact could be the fact that the condition  $t = \tau_2 - \tau_1$  leads to equal evolution times of the electron spin coherence before and after the mixing block  $\pi/2 - T_{mix} - \pi/2$  (orange regions in Fig. 1c). Recall that the artifact at  $t = \tau_2 - \tau_1$  did not appear in the RSE-detected RIDME time traces. This result is consistent with the conjecture above, because if  $\tau_1$  is not equal to  $\tau_2$ , the evolution time of the electron spin coherence before the mixing block is never equal to the evolution time after the mixing block in the RSE-based RIDME sequence (Figure S10).

Having identified the possible reasons for the artifacts, methods for their elimination need to be developed. Based on the proposed origin of the artifact at  $t = \tau_1$ , this artifact can be removed if the effect of dynamical decoupling on the 5p-RIDME time traces will be reduced. To achieve this, a new six-pulse RIDME sequence (6p-RIDME, Fig. 1d) is introduced. The main difference between the two pulse sequences is that the primary echo in the 6p-RIDME is generated by the Carr–Purcell subsequence  $\pi/2 - \tau_1 - \pi - 2\tau_1 - \pi - \tau_1 - echo$  instead of the Hahn echo subsequence  $\pi/2 - \tau_1 - \pi - \tau_1 - echo$ . Evidently, this modification does not aim to avoid dynamical decoupling, but rather provides a condition at which the dynamical decoupling takes place for all  $t$  values instead of a single value  $t = \tau_1$ . To test the efficiency of the new sequence in suppressing this background artifact, 6p-RIDME measurements were performed on **1** using the same parameters as in the 5p-RIDME measurements. The obtained time traces are shown as black lines in Fig. 3. Comparison of these time traces with the corresponding 5p-RIDME time traces reveals that the artifact at  $t = \tau_1$  is significantly reduced. Especially, when  $\tau_{1,ini} \leq 300$  ns, the peak at  $t = \tau_1$  is almost completely suppressed. For larger values of  $\tau_{1,ini}$ , a small peak remains. The remaining peak may be due to the fact that dynamical decoupling is slightly more efficient at  $t = \tau_1$  than at all other  $t$  values, because only at  $t = \tau_1$  the Carr–Purcell subsequence with two inversion pulses plus the mixing block transform into the Carr–Purcell subsequence with three inversion pulses. In turn, increasing the number of inversion pulses in the Carr–Purcell sequence is known to increase the efficiency of dynamical decoupling [48]. Note that, to maximize SNR, one needs to keep  $\tau_1$  as short as possible in the RIDME experiment. In this regard, the fact that the suppression of the  $t = \tau_1$  artifact for  $\tau_{1,ini} > 300$  ns is not as efficient as for  $\tau_{1,ini} \leq 300$  ns is not critical. To avoid the artifact at  $t = \tau_1$ , one needs to use the 6p-RIDME sequence with  $\tau_{1,ini} \leq 300$  ns.

As can be seen from Fig. 3, the second artifact at  $t = \tau_2 - \tau_1$  is also significantly suppressed by the 6p-RIDME sequence. This result was expected because, in the case of 6p-RIDME sequence, the time point  $t = \tau_2 - \tau_1$  does not correspond to equal evolution times before and after the mixing block. Instead, this is achieved at  $t = \tau_2 - 2\tau_1$ . Consequently, all 6p-RIDME time traces contain an additional artifact at  $t = \tau_2 - 2\tau_1$  (blue bars in Fig. 3). Due to the  $^2\text{H-ESEEM}$  averaging, the position of this artifact is distributed over the interval  $t = (\tau_{2,ini} - \tau_{1,ini}, \tau_{2,ini} - 2\tau_{1,ini} - m \cdot \Delta\tau)$ , where  $\tau_{2,ini}$  is the initial value  $\tau_2$ , and the parameters  $\tau_{1,ini}$ ,  $m$ , and  $\Delta\tau$  are defined



above. Since the RIDME time trace is typically acquired using a short  $\tau_{1,ini}$  (e.g.,  $\tau_{1,ini} \leq 300$  ns) and a much longer  $\tau_{2,ini}$  ( $\tau_{2,ini} \gg \tau_{1,ini}$ ), the time point  $t = \tau_2 - 2\tau_1$  appears at the end of the time trace. The artifact at  $t = \tau_2 - 2\tau_1$  can be thus avoided without significant efforts by limiting the  $t$ -axis of the RIDME experiment by  $t_{max} = \tau_{2,ini} - 2\tau_{1,ini} - m \cdot \Delta\tau - \Delta t$ , where  $\Delta t$  is the time in which the artifact decays to zero. Similarly, the artifact at  $t = \tau_2 - \tau_1$  of the 5p-RIDME sequence can be avoided by limiting the  $t$ -axis by  $t_{max} = \tau_{2,ini} - \tau_{1,ini} - \Delta t$ . In our experiments,  $\Delta t$  was about 400 ns. Since the origin of the artifacts at  $t = \tau_2 - 2\tau_1$  and  $t = \tau_2 - \tau_1$  is not fully understood, it is not possible to provide an explanation for the obtained value of  $\Delta t$ . In this regard, further theoretical efforts to explain the origin of these artifacts are important.

In addition, Fig. 3 reveals that almost all 5p-RIDME backgrounds, and especially the corresponding 6p-RIDME backgrounds, exhibit a steeper slope at short  $t$  values ( $t < 100$ – $500$  ns) and a flatter slope at larger  $t$  values. The reasons for this remain unclear and will be studied in the future. Here, the steeper slope at short  $t$  values was considered as being a part of the RIDME background.

Lastly, the influence of the artifacts on the RIDME data analysis was studied for the most relevant case, i.e., when  $\tau_{1,ini} \leq 300$  ns. In this case, the artifacts at  $t = \tau_2 - \tau_1$  and  $t = \tau_2 - 2\tau_1$  can be easily avoided (see above) and only the artifact at  $t = \tau_1$  has to be considered. The Fourier analysis of the 5p- and 6p-RIDME backgrounds is shown in Fig. 4. First, all backgrounds were fitted with a fourth-order polynomial function (red dashed lines in Fig. 4a) and then divided by it. The fourth-order polynomial function was used as the fitting function because it offered the best trade-off between underfitting and overfitting among a number of exponential and polynomial functions tested. Surprisingly, fitting the backgrounds by stretched exponential and third-order polynomial functions, which are commonly used for background correction, resulted in significant underfitting (Figure S12). Second, the background-corrected RIDME time traces were converted to spectra by means of fast Fourier transformation (FFT). All three 5p-RIDME spectra show two prominent features: 1) a small  $^2\text{H}$ -ESEEM peak at 7.8 MHz that remains after the  $^2\text{H}$ -ESEEM averaging, and 2) a more intense, negative peak that occurs in the  $\pm 4.5$  MHz region around the zero frequency (gray lines in Fig. 4b). The latter peak was also observed by Ritsch et al. [20] and is attributed here to the artifact at  $t = \tau_{1,ini}$ . Importantly, this peak almost completely disappears when the 6p-RIDME sequence is used (black lines in Fig. 4b).

### 3.2 RIDME Measurements on the Nitroxide Biradical

Nitroxide biradical **2** was used as a second model system to investigate the effect of the RIDME background artifacts on the extracted distance distributions and to test the performance of the 6p-RIDME sequence. Note that RIDME is rarely used to measure nitroxide–nitroxide distance distributions, because PELDOR outperforms RIDME in terms of modulation depth and SNR for this particular spin pair [1]. Nevertheless, to model the situation at which the background artifacts become pronounced in the RIDME time trace, a large RIDME modulation depth is not needed and even deliberately avoided here.

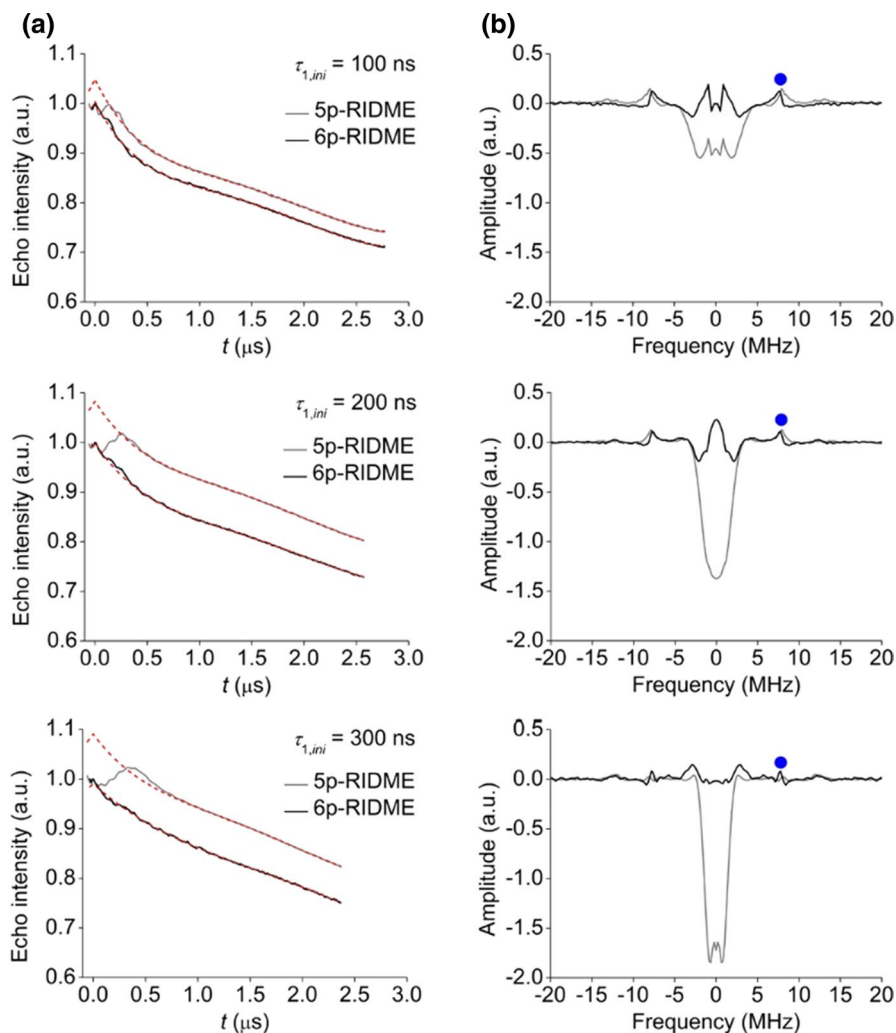


**Fig. 4** Fourier analysis of the RIDME time traces of **1**. **a** 5p-RIDME (gray lines) and 6p-RIDME (black lines) time traces and their fourth-order polynomial fits (red dashed lines). **b** The corresponding 5p-RIDME (gray lines) and 6p-RIDME (black lines) spectra. The position of the remaining  $^2\text{D}$  ESEEM peak is marked by a dot (color figure online)

5p- and 6p-RIDME time traces of **2** were measured at 50 K with  $\tau_{1,ini} = 100, 200,$  and  $300$  ns (Fig. 5a, rows 1–3 and 5–8). In addition, the 5p-RIDME time trace of **2** was also acquired with  $\tau_{1,ini} = 4$   $\mu\text{s}$ , corresponding to the case  $\tau_{1,ini} > \tau_{2,ini}$  (Fig. 5a, row 4). All time traces were background corrected with a fourth-order polynomial function (red dashed lines in Fig. 5a). The resulting time traces are shown in Fig. 5b. The 5p-RIDME time traces measured with  $\tau_{1,ini}$  of 100–300 ns are strongly affected by the  $t = \tau_1$  artifact, which can be seen as a broad peak over the first few periods of the dipolar oscillation (Fig. 5b, rows 1–3). After the Fourier transform, the artifact

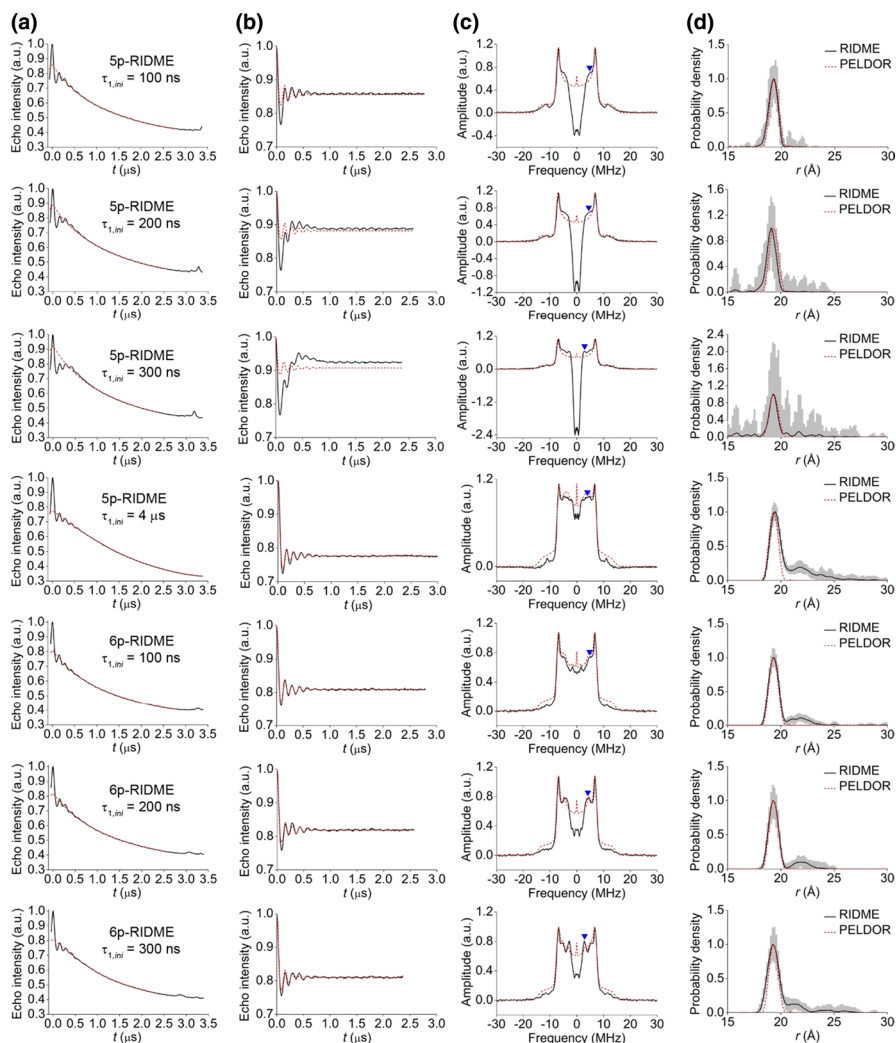


**Fig. 5** Q-band RIDME measurements of the inter-nitroxide distance distribution in **2**. **a** 5p and 6p-RIDME time traces (black lines) and their fourth-order polynomial fits (red dashed lines). **b** The background-corrected 5p- and 6p-RIDME time traces (black lines) and their *DeerAnalysis* fits (red dashed lines). **c** The 5p- and 6p-RIDME spectra (black lines) and their *DeerAnalysis* fits (red dashed lines). Components of the spectra that cause the distance artifacts are marked by triangles. **d** The *DeerAnalysis*-based inter-nitroxide distance distributions (black lines) and their confidence intervals (gray shades). The PELDOR-based inter-nitroxide distance distribution taken from Ref. [44] is shown as a dashed line (color figure online)

gives rise to a large negative peak around the zero frequency (Fig. 5c, rows 1–3), in complete analogy to the one obtained for monoradical **1**. In the presence of this artifact, accurate background correction becomes difficult, leading to different values of modulation depth for different  $\tau_{1,ini}$  (Fig. 5b, rows 1–3). In contrast, the 5p-RIDME time trace measured with  $\tau_{1,ini}=4\ \mu\text{s}$  shows no traces of the  $t=\tau_1$  artifact. This

artifact is also strongly suppressed in the 6p-RIDME time traces, as indicated by the absence of the negative peak around the zero frequency in the corresponding spectra (Fig. 5c, rows 4–8). Small residuals of the artifact can still be seen in the 6p-RIDME time traces recorded with  $\tau_{1,ini}$  of 200 and 300 ns, which makes the minimum around the zero frequency in the corresponding spectra slightly deeper than usual. Nevertheless, it can be seen that the 6p-RIDME sequence clearly suppressed the artifact, which is also reflected in the consistent modulation depth for all  $\tau_{1,ini}$  values used.

Next, the inter-nitroxide distance distribution was extracted from the background-corrected time traces using *DeerAnalysis*. For all 5p-RIDME time traces containing the  $t = \tau_1$  artifact, it turned out to be impossible to obtain a good fit (Fig. 5b, rows 1–3), and consequently the uncertainty ranges of the extracted distances were large (gray shades in Fig. 5d, rows 1–3). Nevertheless, the expected distance peak at about 19 Å was still correctly determined in the case of  $\tau_{1,ini} = 100$  ns. In the case of  $\tau_{1,ini} = 200$  ns, the significant part of the expected distance peak is below the uncertainty range, and in the case of  $\tau_{1,ini} = 300$  ns, the entire distance distribution falls within the uncertainty range. In contrast, *DeerAnalysis* provided good fits (Fig. 5b, rows 4–8) and distance distributions with better precision (Fig. 5d, rows 4–8) for all 6p-RIDME time traces, as well as the 5p-RIDME time trace recorded with  $\tau_{1,ini} = 4$   $\mu$ s. However, in addition to the expected, most intense peak, the corresponding distance distributions contain an unexpected distance peak of weak intensity in the range of 20–25 Å (Fig. 5d, rows 4–8). A large part of this peak falls within the uncertainty range, suggesting that it is most likely an artifact. This is also suggested by the fact that the position of this distance peak depends on the  $\tau_{1,ini}$  value. The component of the RIDME spectra that gives rise to the distance artifact is marked by the triangle in Fig. 5c. Note that this component is present in both, 5p- and 6p-RIDME spectra. The only reason why this component does not lead to the distance artifact in 5p-RIDME data acquired with  $\tau_{1,ini} \leq 300$  ns is an overall low quality of the *DeerAnalysis* fits obtained for the corresponding time traces. The reasons causing the distance artifact are unclear. It could be due to imperfections of background correction or insufficient ESEEM suppression, especially of small hyperfine couplings.

With the exception of the small distance artifact, the inter-nitroxide distance distributions obtained with 6p-RIDME are in a good agreement with the distance distribution obtained with PELDOR. In principle, some of the distance distributions obtained with 5p-RIDME are also in an overall agreement with the PELDOR results, but the precision of these distributions is much lower compared to 6p-RIDME. Thus, the capability of the 6p-RIDME sequence to suppress the  $t = \tau_1$  artifact is an important factor for the accurate extraction of distance distributions from RIDME data.

### 3.3 RIDME Measurements on Fe(III)-Nitroxide Model Compounds

In the final test, the performance of 5p-RIDME and 6p-RIDME was compared for the low-spin Fe<sup>3+</sup>-nitroxide model compounds **3** and **4**. The 5p-RIDME measurements on **3** and **4** were described in our previous publication [34]. Here, the same

samples and the same parameters were used to record the 6p-RIDME time traces. An overlay of the 5p- and 6p-RIDME time traces of **3** and **4** is shown in Fig. 6a. After background correction, the shape and modulation depth of the 6p-RIDME time traces barely different from the shape and modulation depth of the corresponding 5p-RIDME time traces (Fig. 6b). The corresponding RIDME spectra differ only in the range  $\pm 2$  MHz around the zero frequency, where the 5p-RIDME spectra show a slightly deeper minimum due to the  $t = \tau_1$  artifact (Fig. 6c). Because of the similarity of the 5p- and 6p-RIDME time traces, the analysis of these time traces using the program *AnisoDipFit* yielded nearly identical distance and angle distributions and the corresponding confidence intervals (see SI, Chapter 6). Based on these results, one can conclude that the influence of the  $t = \tau_1$  artifact on the 5p- and 6p-RIDME data of **3** and **4** is negligible. This is likely due to the fact that deuterated THF was used as the solvent for **3** and **4** instead of TES buffer. As shown above for **1**, the intensity of the  $t = \tau_1$  artifact is significantly lower in deuterated THF than that in deuterated TES buffer (see Figure S8). The measurements on **3** and **4** in TES buffer could not be done, because neither of these compounds is soluble in TES buffer. Another reason may be the larger modulation depths obtained for **3** and **4** as compared to those for **2**.

## 4 Conclusions

5p-RIDME background artifacts were systematically investigated on several test systems, which provided insight into the possible origin of these artifacts. One of the artifacts was assigned to the effect of dynamical decoupling at the time point  $t = \tau_1$ . Another artifact was shown to appear only when the evolution times of the electron spin coherence before and after the mixing block were the same. In the 5p-RIDME sequence with refocused virtual echo detection, this condition is realized at the time

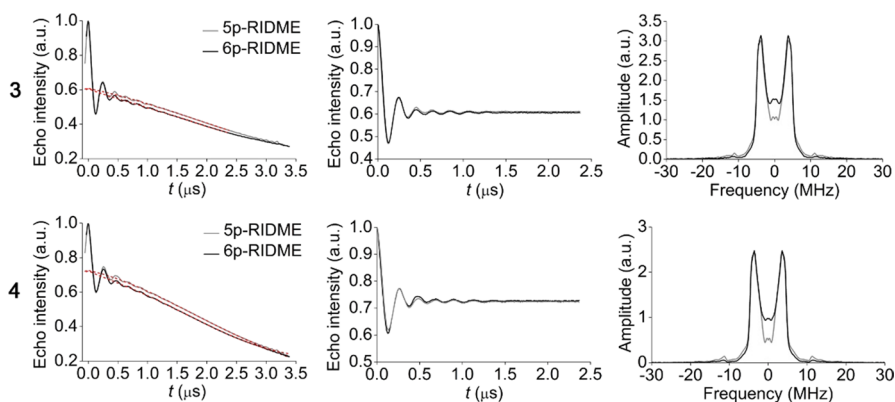


**Fig. 6** Q-band RIDME measurements of the low-spin  $\text{Fe}^{3+}$ -nitroxide distance distribution in **3** (top row) and **4** (bottom row). **a** 5p-RIDME (gray lines) and 6p-RIDME (black lines) time traces and their fourth-order polynomial fits (red dashed lines). **b** The background-corrected 5p- (gray lines) and 6p-RIDME (black lines) time traces and **c** the corresponding spectra (color figure online)

point  $t = \tau_2 - \tau_1$ . The intensity of both artifacts was shown to depend on the type of solvent. Among the three tested solvents tested, the highest artifact intensity was obtained for deuterated TES buffer, and the lowest intensity for deuterated THF. To suppress the first artifact, a new 6p-RIDME sequence was introduced. The efficiency of this sequence was confirmed on several examples. The second artifact occurred at the end of the 5p- and 6p-RIDME time traces and could, therefore, be easily avoided by limiting the time axis of the time traces. Alternatively, the second artifact can be avoided using the 5p-RIDME sequence with refocused stimulated echo detection.

The 5p-RIDME measurements on the nitroxide biradical demonstrated the importance of removing the background artifacts before converting the time traces into the distance distributions. This goal was achieved when the 6p-RIDME sequence was used. Despite this improvement, the distance distributions extracted from both the 5p- and 6p-RIDME time traces were found to contain a distance artifact that is not present in the corresponding PELDOR-based distance distribution. The origin of this artifact is unclear and needs to be explored in the future.

In contrast, the background artifacts were shown to have a small effect on both the 5p- and 6p-RIDME time traces of the low-spin  $\text{Fe}^{3+}$ -nitroxide model compounds. This was attributed to the solvent effect, as well as to the influence of the background artifacts on the RIDME data becoming smaller as the RIDME modulation depth increases.

**Supplementary Information** The online version contains supplementary material available at <https://doi.org/10.1007/s00723-021-01326-1>.

**Acknowledgements** We thank Prof. Gunnar Jeschke and Maxim Yulikov for helpful discussions.

**Funding** Open Access funding enabled and organized by Projekt DEAL.

**Open Access** This article is licensed under a Creative Commons Attribution 4.0 International License, which permits use, sharing, adaptation, distribution and reproduction in any medium or format, as long as you give appropriate credit to the original author(s) and the source, provide a link to the Creative Commons licence, and indicate if changes were made. The images or other third party material in this article are included in the article's Creative Commons licence, unless indicated otherwise in a credit line to the material. If material is not included in the article's Creative Commons licence and your intended use is not permitted by statutory regulation or exceeds the permitted use, you will need to obtain permission directly from the copyright holder. To view a copy of this licence, visit <http://creativecommons.org/licenses/by/4.0/>.

## References

1. C.R. Timmel, J.R. Harmer (eds.), *Structure and Bonding, Structural Information from Spin-Labels and Intrinsic Paramagnetic Centres in the Biosciences* (Springer, Berlin, 2013)
2. A.D. Milov, K.M. Salikhov, M.D. Shchirov, Use of the double resonance in electron spin echo method for the study of paramagnetic center spatial distribution in solids. *Fiz. Tverd. Tela* **23**, 975 (1981)
3. R.E. Martin, M. Pannier, F. Diederich, V. Gramlich, M. Hubrich, H.W. Spiess, Dead-time free measurement of dipole-dipole interactions between electron spins. *Angew. Chemie Int. Ed.* **37**, 2833 (1998)
4. S. Saxena, J.H. Freed, Double quantum two-dimensional Fourier transform electron spin resonance: Distance measurements. *Chem. Phys. Lett.* **251**, 102 (1996)

5. G. Jeschke, M. Pannier, A. Godt, H.W. Spiess, Dipolar spectroscopy and spin alignment in electron paramagnetic resonance. *Chem. Phys. Lett.* **331**, 243 (2000)
6. L.V. Kulik, S.A. Dzuba, I.A. Grigoryev, Y.D. Tsvetkov, Electron dipole-dipole interaction in ESEEM of nitroxide biradicals. *Chem. Phys. Lett.* **343**, 315 (2001)
7. S. Milikisyants, F. Scarpelli, M.G. Finiguerra, M. Ubbink, M. Huber, A pulsed EPR method to determine distances between paramagnetic centers with strong spectral anisotropy and radicals: the dead-time free RIDME sequence. *J. Magn. Reson.* **201**, 48 (2009)
8. O. Schiemann, T.F. Prisner, Long-range distance determinations in biomacromolecules by EPR spectroscopy. *Q. Rev. Biophys.* **40**, 1 (2007)
9. B. Joseph, A. Sikora, E. Bordignon, G. Jeschke, D.S. Cafiso, T.F. Prisner, Distance measurement on an endogenous membrane transporter in *E. coli* cells and native membranes using EPR spectroscopy. *Angew. Chemie Int. Ed.* **54**, 6196 (2015)
10. A. Martorana, G. Bellapadrona, A. Feintuch, E. Di Gregorio, S. Aime, D. Goldfarb, Probing protein conformation in cells by EPR distance measurements using  $Gd^{3+}$  spin labeling. *J. Am. Chem. Soc.* **136**, 13458–13465 (2014)
11. N. Fleck, C.A. Heubach, T. Hett, F.R. Haege, P.P. Bawol, H. Baltruschat, O. Schiemann, SLIM: A short-linked, highly redox-stable trityl label for high-sensitivity in-cell EPR distance measurements. *Angew. Chemie Int. Ed.* **59**, 9767 (2020)
12. P. Widder, J. Schuck, D. Summerer, M. Drescher, Combining site-directed spin labeling in vivo and in-cell EPR distance determination. *Phys. Chem. Chem. Phys.* **22**, 4875 (2020)
13. G. Jeschke, Dipolar spectroscopy – double-resonance methods. *EMagRes* **5**, 1459 (2016)
14. P.P. Borbat, J.H. Freed, Dipolar spectroscopy – single-resonance methods. *EMagRes* **6**, 465 (2017)
15. G.W. Reginsson, N.C. Kunjir, S.T. Sigurdsson, O. Schiemann, Trityl radicals: spin labels for nanometer-distance measurements. *Chem. A Eur. J.* **18**, 13580 (2012)
16. J.J. Jassoy, A. Berndhäuser, F. Duthie, S.P. Kühn, G. Hagelueken, O. Schiemann, Versatile trityl spin labels for nanometer distance measurements on biomolecules in vitro and within cells. *Angew. Chemie Int. Ed.* **56**, 177 (2017)
17. J.J. Jassoy, C.A. Heubach, T. Hett, F. Bernhard, F.R. Haege, G. Hagelueken, O. Schiemann, Site selective and efficient spin labeling of proteins with a maleimide-functionalized trityl radical for pulsed dipolar EPR spectroscopy. *Molecules* **24**, 2735 (2019)
18. A. Meyer, D. Abdullin, G. Schnakenburg, O. Schiemann, Single and double nitroxide labeled bis(terpyridine)-copper(II): influence of orientation selectivity and multispin effects on PELDOR and RIDME. *Phys. Chem. Chem. Phys.* **18**, 9262 (2016)
19. A. Giannoulis, M. Oranges, B.E. Bode, Monitoring complex formation by relaxation-induced pulse electron paramagnetic resonance distance measurements. *ChemPhysChem* **18**, 2318 (2017)
20. I. Ritsch, H. Hintz, G. Jeschke, A. Godt, M. Yulikov, Improving the accuracy of Cu(II)–nitroxide RIDME in the presence of orientation correlation in water-soluble Cu(II)–nitroxide rulers. *Phys. Chem. Chem. Phys.* **21**, 9810 (2019)
21. J.L. Wort, K. Ackermann, A. Giannoulis, A.J. Stewart, D.G. Norman, B.E. Bode, Sub-Micromolar pulse dipolar EPR spectroscopy reveals increasing  $Cu^{II}$  -labelling of double-histidine motifs with lower temperature. *Angew. Chemie Int. Ed.* **58**, 11681 (2019)
22. D.M. Engelhard, A. Meyer, A. Berndhäuser, O. Schiemann, G.H. Clever, Di-copper(II) DNA G-quadruplexes as EPR distance rulers. *Chem. Commun.* **54**, 7455 (2018)
23. F.D. Breitgoff, K. Keller, M. Qi, D. Klose, M. Yulikov, A. Godt, G. Jeschke, UWB DEER and RIDME distance measurements in Cu(II)–Cu(II) spin pairs. *J. Magn. Reson.* **308**, 106560 (2019)
24. K. Keller, M. Qi, C. Gmeiner, I. Ritsch, A. Godt, G. Jeschke, A. Savitsky, M. Yulikov, Intermolecular background decay in RIDME experiments. *Phys. Chem. Chem. Phys.* **21**, 8228 (2019)
25. S. Razzaghi, M. Qi, A.I. Nalepa, A. Godt, G. Jeschke, M. Yulikov, RIDME spectroscopy with Gd(III) centers. *J. Phys. Chem. Lett.* **5**, 3970 (2014)
26. K. Keller, A. Doll, M. Qi, A. Godt, G. Jeschke, M. Yulikov, Averaging of nuclear modulation artefacts in RIDME experiments. *J. Magn. Reson.* **272**, 108 (2016)
27. A. Collauto, V. Frydman, M.D. Lee, E.H. Abdelkader, A. Feintuch, J.D. Swarbrick, B. Graham, G. Otting, D. Goldfarb, RIDME distance measurements using Gd(III) tags with a narrow central transition. *Phys. Chem. Chem. Phys.* **18**, 19037 (2016)
28. K. Keller, V. Mertens, M. Qi, A.I. Nalepa, A. Godt, A. Savitsky, G. Jeschke, M. Yulikov, Computing distance distributions from dipolar evolution data with overtones: RIDME spectroscopy with Gd(III)-based spin labels. *Phys. Chem. Chem. Phys.* **19**, 17856 (2017)

29. A. Meyer, O. Schiemann, PELDOR and RIDME measurements on a high-spin manganese(II) bisnitroxide model complex. *J. Phys. Chem. A* **120**, 3463 (2016)
30. K. Keller, M. Zalibera, M. Qi, V. Koch, J. Wegner, H. Hintz, A. Godt, G. Jeschke, A. Savitsky, M. Yulikov, EPR characterization of Mn(II) complexes for distance determination with pulsed dipolar spectroscopy. *Phys. Chem. Chem. Phys.* **18**, 25120 (2016)
31. A. Giannoulis, C.L. Motion, M. Oranges, M. Bühl, G.M. Smith, B.E. Bode, Orientation selection in high-field RIDME and PELDOR experiments involving low-spin Co(II) ions. *Phys. Chem. Chem. Phys.* **20**, 2151 (2018)
32. A.V. Astashkin, B.O. Elmore, W. Fan, J.G. Guillemette, C. Feng, Pulsed ENDOR determination of relative orientation of g-frame and molecular frame of imidazole-coordinated heme center of iNOS. *J. Am. Chem. Soc.* **132**, 12059 (2010)
33. D. Abdullin, F. Duthie, A. Meyer, E.S. Müller, G. Hagelueken, O. Schiemann, Comparison of PELDOR and RIDME for distance measurements between nitroxides and low-spin Fe(III) ions. *J. Phys. Chem. B* **119**, 13539 (2015)
34. D. Abdullin, P. Brehm, N. Fleck, S. Spicher, S. Grimme, O. Schiemann, Pulsed EPR dipolar spectroscopy on spin pairs with one highly anisotropic spin center: the low-spin Fe<sup>III</sup> case. *Chem. A Eur. J.* **25**, 14388 (2019)
35. D. Abdullin, H. Matsuoka, M. Yulikov, N. Fleck, C. Klein, S. Spicher, G. Hagelueken, S. Grimme, A. Luetzen, O. Schiemann, Pulsed EPR dipolar spectroscopy under the breakdown of the high-field approximation: the high-spin iron(III) case. *Chem. A Eur. J.* **25**, 8820 (2019)
36. A.V. Astashkin, Mapping the structure of metalloproteins with RIDME. *Methods Enzymol.* **563**, 251 (2015)
37. D. Abdullin, O. Schiemann, Pulsed dipolar EPR spectroscopy and metal ions: methodology and biological applications. *ChemPlusChem* **85**, 353 (2020)
38. A.M. Bowen, C.E. Tait, C.R. Timmel, J.R. Harmer, Orientation-selective DEER using rigid spin labels, cofactors, metals, and clusters, in *Structure and Bonding, Structural Information from Spin-Labels and Intrinsic Paramagnetic Centres in the Biosciences*, ed. by C.R. Timmel, J.R. Harmer (Springer, Berlin, 2013), p. 152
39. Z. Wu, A. Feintuch, A. Collauto, L.A. Adams, L. Aurelio, B. Graham, G. Otting, D. Goldfarb, Selective distance measurements using triple spin labeling with Gd<sup>3+</sup>, Mn<sup>2+</sup>, and a nitroxide. *J. Phys. Chem. Lett.* **8**, 5277 (2017)
40. M. Yulikov, Spectroscopically orthogonal spin labels and distance measurements in biomolecules. *Electron Paramagn. Reson.* **24**, 1 (2015)
41. D. Abdullin, N. Florin, G. Hagelueken, O. Schiemann, Localization of metal ions in biomolecules by means of pulsed dipolar EPR spectroscopy. *Angew. Chemie Int. Ed.* **54**, 1827 (2015)
42. A. Gamble Jarvi, T.F. Cunningham, S. Saxena, Efficient localization of a native metal ion within a protein by Cu<sup>2+</sup>-based EPR distance measurements. *Phys. Chem. Chem. Phys.* **21**, 10238 (2019)
43. B.E. Bode, J. Plackmeyer, T.F. Prisner, O. Schiemann, PELDOR measurements on a nitroxide-labeled Cu(II) porphyrin: orientation selection, spin-density distribution, and conformational flexibility. *J. Phys. Chem. A* **112**, 5064 (2008)
44. D. Abdullin, N. Fleck, C. Klein, P. Brehm, S. Spicher, A. Lützen, S. Grimme, O. Schiemann, Synthesis of  $\mu_2$ -oxo-bridged iron(III) tetraphenylporphyrin-spacer-nitroxide dimers and their structural and dynamics characterization by using EPR and MD simulations. *Chem. A Eur. J.* **25**, 2586 (2019)
45. G. Jeschke, V. Chechik, P. Ionita, A. Godt, H. Zimmermann, J. Banham, C.R. Timmel, D. Hilger, H. Jung, DeerAnalysis2006 – a comprehensive software package for analyzing pulsed ELDOR data. *Appl. Magn. Reson.* **30**, 473 (2006)
46. D. Abdullin, AnisoDipFit: simulation and fitting of pulsed EPR dipolar spectroscopy data for anisotropic spin centers. *Appl. Magn. Reson.* **51**, 725 (2020)
47. H.Y. Carr, E.M. Purcell, Effects of diffusion on free precession in nuclear magnetic resonance experiments. *Phys. Rev.* **94**, 630 (1954)
48. J. Soetbeer, M. Hülsmann, A. Godt, Y. Polyhach, G. Jeschke, Dynamical decoupling of nitroxides in o-terphenyl: a study of temperature, deuteration and concentration effects. *Phys. Chem. Chem. Phys.* **20**, 1615 (2018)